ACS OMEGA

http://pubs.acs.org/journal/acsodf

Article

Inorganic Lead-Free B-γ-$CsSnI_3$ Perovskite Solar Cells Using Diverse Electron-Transporting Materials: A Simulation Study

Shuo Lin, Baoping Zhang, Tie-Yu Lü, Jin-Cheng Zheng,* Huaqing Pan, Huanting Chen, Chuanjin Lin, Xirong Li, and Jinrong Zhou

Cite This: *ACS Omega* 2021, 6, 26689–26698

Read Online

ACCESS | Metrics & More | Article Recommendations | Supporting Information

ABSTRACT: B-γ-$CsSnI_3$ perovskite solar cells (PSCs) are simulated employing diverse electron-transporting layers (ETLs, including TiO_2, ZnO, SnO_2, GaN, C_{60}, and PCBM), and a comparative study has been made. Both regular and inverted planar structures are simulated. Effects of the thickness of absorbers and ETLs, doping of ETLs, and interface trap states on the photovoltaic performance are studied to optimize the device structures. The regular structures have larger short-circuit current density (J_{sc}) than the inverted structures, but the inverted structures have larger fill factor (FF). All of the simulated optimal PSCs have similar open-circuit voltages (V_{oc}) of ~0.96 V. The PSCs with TiO_2 ETLs have the best photovoltaic performance, and the optimum structure exhibits the highest efficiency of 20.2% with a V_{oc} of 0.97 V, J_{sc} of 29.67 mA/cm^2, and FF of 0.70. The optimal PSCs with ZnO, GaN, C_{60}, and PCBM ETLs exhibit efficiencies of 17.88, 18.09, 16.71, and 16.59%, respectively. The optimal PSC with SnO_2 ETL exhibits the lowest efficiency of 15.5% in all of the simulated PSCs due to its cliff-like band offset at the SnO_2/$CsSnI_3$ interface. Furthermore, the increase of interface trap density and capture cross section is found to reduce the photovoltaic performance of PSCs. This work contributes to designing and fabricating $CsSnI_3$ PSCs.

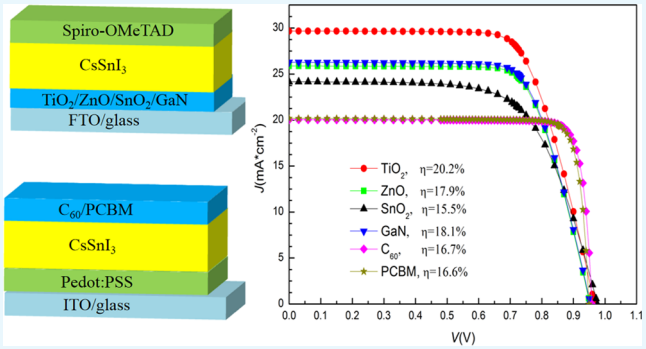

1. INTRODUCTION

Perovskite solar cells (PSCs) have emerged as a breakthrough photovoltaic (PV) technology, holding unprecedented promise for high-efficiency, low-cost solar cells due to their excellent photoelectric properties.[1−5] However, the potential toxicity associated with the lead-containing PSCs has become a major concern. The primary drawback of Pb perovskites for solar cells is that soluble Pb compounds are well known to be toxic to both the natural environment and humans. Therefore, there has been growing interest in the development of alternative perovskites that use Sn instead of Pb, such as $CsSnI_3$. Tin-based halide perovskite materials have been successfully employed in lead-free perovskite solar cells. Recently, several studies have revealed that the substitution of the methylammonium cation by cesium (Cs) in the perovskite structure could significantly enhance its thermal stability.[6]

The B-γ-$CsSnI_3$ perovskite has been studied comprehensively and shown to possess favorable photoelectric properties for PV application. B-γ-$CsSnI_3$ has a direct band gap of ≈1.3 eV,[6] which is suitable for solar radiation, high absorption coefficient (≈10^4 cm^{-1} in the visible region),[6] and high charge-carrier mobility (~400 cm^2/(V·s) for holes).[7] B-γ-$CsSnI_3$ has low exciton binding energy (10−20 meV,[6] Wannier-type excitons), so the carrier separation in $CsSnI_3$ is easier than that in typical organic absorbers.[8] In addition, several studies[6,7,9] have shown that the $CsSnI_3$ has a melting point of 451 °C, and it can be synthesized via melting−solidification, implying superior intrinsic thermal stability. By contrast, the halide perovskite analogues of $MASnI_3$ and $FASnI_3$ start to decompose at ≈200 °C.[6] Most of the reported power conversion efficiencies (PCEs) for $CsSnI_3$-based PSCs are between 3 and 5%.[10,11] Very recently, Li et al.[12] reported a PCE of 8.2% (January 2021) for $CsSnI_3$ PSCs, and Ye et al.[13] reported PCEs of 10.1 and 9.6% (March 2021). It is remarkable that the PCE of 10.1% is the highest one among all of the lead-free all-inorganic perovskite solar cells reported so far.[12,13] The aforementioned considerations provide the rationale for the study of B-γ-$CsSnI_3$ as a promising inorganic, lead-free, thermally stable perovskite for next-generation PSCs.

Dopant concentration, thickness, mobility and lifetime of carriers, surface properties, etc., of the electron-transporting layer (ETL) and hole transporting layer (HTL) and band alignment with perovskites are crucial factors for the transport of charge carriers to the front and back contacts.[14] There have been

Received: August 1, 2021
Accepted: September 14, 2021
Published: September 29, 2021

many reports on HTL-free PSCs with high performance,[15−18] but very few reports on ETL-free PSCs with high performance have been found till now.[19] Therefore, it seems that ETLs are essential and necessary for PSCs, at least so far.[19] Theoretical and simulation studies could help to gain a deep insight into the transport mechanism of ETLs[20] and select the appropriate electron-transporting materials for $CsSnI_3$ PSCs. In addition, simulations could help to find the optimal device structures and provide the theoretical possibilities of design for $CsSnI_3$ PSCs. However, to the best of our knowledge, there has been no theoretical and simulation literature on the comparative study of electron-transporting materials for $CsSnI_3$ PSCs so far.

In this work, B-γ-$CsSnI_3$ is used as an all-inorganic lead-free absorber for PSCs. Several inorganic and organic semiconductors (TiO_2, ZnO, SnO_2, GaN, C_{60}, and PCBM) are adopted as ETLs for $CsSnI_3$ PSCs. A comparative study on these electron-transporting materials has been made to select the appropriate electron-transporting materials. Both regular and inverted planar structures are simulated. Effects of the thickness of $CsSnI_3$ and ETLs and the dopant concentration of ETLs on the photovoltaic performance of PSCs are investigated to optimize the device structures for $CsSnI_3$ PSCs and provide the theoretical possibilities of design for $CsSnI_3$ PSCs. On the basis of comparing the photovoltaic performance of the optimal PSCs with those ETLs, the possible reasons (band structures, material, and device parameters) behind the discrepancies of performance are investigated and discussed in detail, to provide guidance for designing $CsSnI_3$ PSCs. In addition, the effects of interface trap density of states are also studied.

2. MODELING AND SIMULATIONS

The exciton in typical organic absorbers is of Frenkel-type; therefore, the exciton binding energy has to be taken into account for the carrier separation for accurate PV device modeling, which is rather complicated.[8] In contrast, the exciton in the $CsSnI_3$ perovskite is of typical Wannier-type, so the photoexcited carriers can be dealt with in the same manner as with inorganic materials. The two facts, i.e., structural similarity without the mesoporous structure and the exciton type, enable us to apply an existing device simulator widely used in inorganic solar cells to the perovskite solar cells.[8]

In this study, AMPS-1D software[21] is used to simulate $CsSnI_3$ PSCs. AMPS-1D is a one-dimensional device physics code and based on the basic equations of semiconductors and solar cells.[21] We have successfully applied this code in the simulation of $In_xGa_{1-x}N$/SnS and $Al_xGa_{1-x}N$/SnS heterojunction solar cells.[22] Here, we briefly describe the main equations used in the simulation as follows. Poisson's equation:

$$\frac{\mathrm{d}}{\mathrm{d}x}\left[\varepsilon(x)\frac{\mathrm{d}\Psi(x)}{\mathrm{d}x}\right] = q^2 \times [p(x) - n(x) + N_D^+(x) - N_A^-(x) + p_t(x) - n_t(x)] \quad (1)$$

where the local vacuum level (in the unit of eV), absolute dielectric constant and the free electron n, free hole p, trapped electron n_t and trapped hole p_t, as well as the ionized donor-like doping N_D^+ and ionized acceptor-like doping N_A^- concentrations are all functions of the position coordinate x. q is the electron charge. The continuity equation for electrons is as follows:

$$\frac{1}{q}\left[\frac{\mathrm{d}J_n(x)}{\mathrm{d}x}\right] = -G_L(x) + R(x) \quad (2)$$

The continuity equation for holes is as follows:

$$\frac{1}{q}\left[\frac{\mathrm{d}J_p(x)}{\mathrm{d}x}\right] = G_L(x) - R(x) \quad (3)$$

$J_n(x) = n\mu_n \frac{\mathrm{d}E_f^n(x)}{\mathrm{d}x}$ and $J_p(x) = p\mu_p \frac{\mathrm{d}E_f^p(x)}{\mathrm{d}x}$ are the electron and hole current densities, respectively. μ_n and μ_p are the mobilities of the electron and hole, respectively. E_f^n and E_f^p are the electron and hole quasi-Fermi levels, respectively. $R(x)$ is the net recombination rate resulting from direct (band-to-band) recombination and indirect (Shockley−Read−Hall) recombination traffic through gap states. $G_L(x)$ is the optical generation rate.

Determining transport characteristics then becomes a task of solving the three coupled nonlinear differential equations (eqs 1−3), each of which has two associated boundary conditions. In AMPS, these three coupled equations are solved simultaneously to obtain a set of three unknown state variables at each point in the device: the local vacuum level and the electron and hole quasi-Fermi levels. From these three state variables, the free carrier concentrations $\left(n(x) = \frac{2}{\sqrt{\pi}} N_c F_{1/2}\left[-\frac{E_c(x) - E_F^n(x)}{kT}\right]\right.$ and $\left.p(x) = \frac{2}{\sqrt{\pi}} N_v F_{1/2}\left[-\frac{E_F^p(x) - E_v(x)}{kT}\right]\right)$, where N_c and N_v are the effective density of states in the conduction band and the valence band, respectively; k is the Boltzmann constant, T the temperature, and $F_{1/2}(\xi)$ the Fermionic integral), fields $\left(E(x) = \frac{1}{q}\frac{\mathrm{d}\Psi(x)}{\mathrm{d}x}\right)$, currents, etc. can then be computed.

The structures of regular and inverted planar $CsSnI_3$ PSCs are shown in Figure 1. The material parameters of $CsSnI_3$, ETLs, and HTLs used in the simulations are shown in Table S1. The

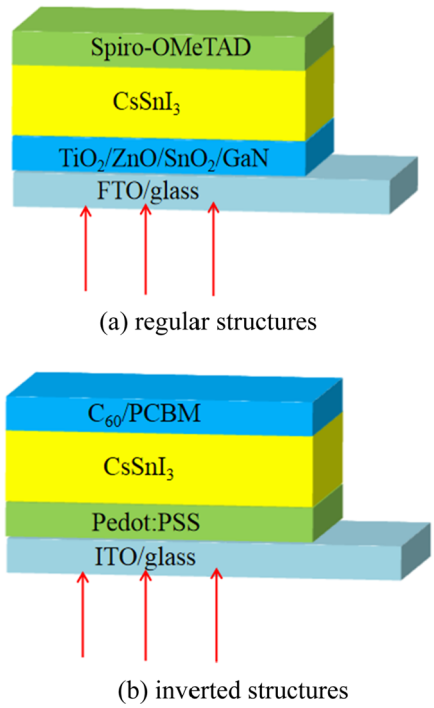

Figure 1. Structures of $CsSnI_3$ perovskite solar cells.

https://doi.org/10.1021/acsomega.1c04096
ACS Omega 2021, 6, 26689−26698

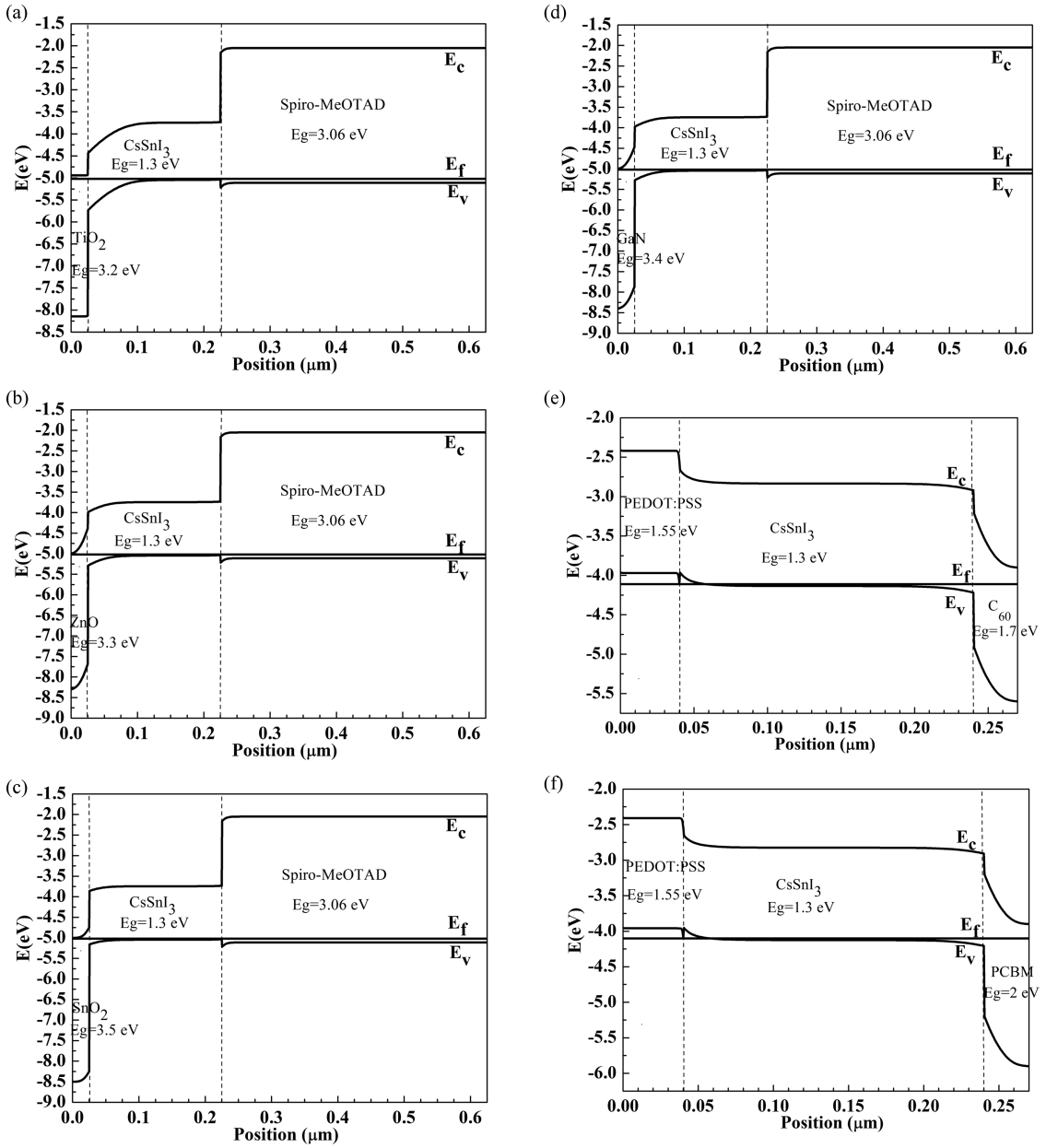

Figure 2. Band structures of $CsSnI_3$ PSCs. $CsSnI_3$ PSC with ETL TiO_2 (a), ZnO (b), SnO_2 (c), GaN (d), C_{60} (e), and PCBM (f).

lifetime model is adopted in this work except that the density of states (DOS) model is used in the simulation of interface trap density of states. The simulation is performed under AM1.5G illumination (100 mW/cm^2, 0.32−1.32 μm). Following are the simulation procedures carried out to understand the behavior and role of ETLs:

(a) The band structures.
(b) The effect of thickness of absorber.
(c) The effect of thickness and dopant concentration of ETLs.
(d) Comparison of the photovoltaic performance for the best structures.
(e) The effect of interface trap density of states.

3. RESULTS AND DISCUSSION

3.1. Band Structures. The band alignment of all contact materials and $CsSnI_3$ adopted in this study is shown in Figure S1, and the initial thickness and donor concentrations of ETLs are shown in Table S1. The band structures of all of the simulated PSCs are shown in Figure 2. As the band gap (E_g) and electron affinity (χ) of TiO_2, ZnO, and GaN are very close, the band structures of PSCs with TiO_2, ZnO, and GaN are similar. For all of the simulated PSCs, there is no spike-like band offset in the conduction band at the ETL/$CsSnI_3$ interface, which can form an electron barrier to block the drift of photogenerated electrons from $CsSnI_3$ absorbers and lead to the degraded collection efficiency. Besides, the valence band offset at the ETL/$CsSnI_3$ interface can generate a hole barrier to prevent the hole in $CsSnI_3$ from moving to ETLs. However, as the electron affinity of SnO_2 is too large for the PSC with SnO_2, there are cliff-like band offsets in the conduction band at the SnO_2/$CsSnI_3$ interface ($\Delta E_c = \chi(CsSnI_3) - \chi(SnO_2) = 3.62 - 4.5 = -0.88$ eV, $\Delta E_v = \Delta E_c + E_g(CsSnI_3) - E_g(SnO_2) = -0.88 + 1.3 - 3.5 = -3.08$ eV), which can give rise to high interface-related recombination.[23]

https://doi.org/10.1021/acsomega.1c04096
ACS Omega 2021, 6, 26689−26698

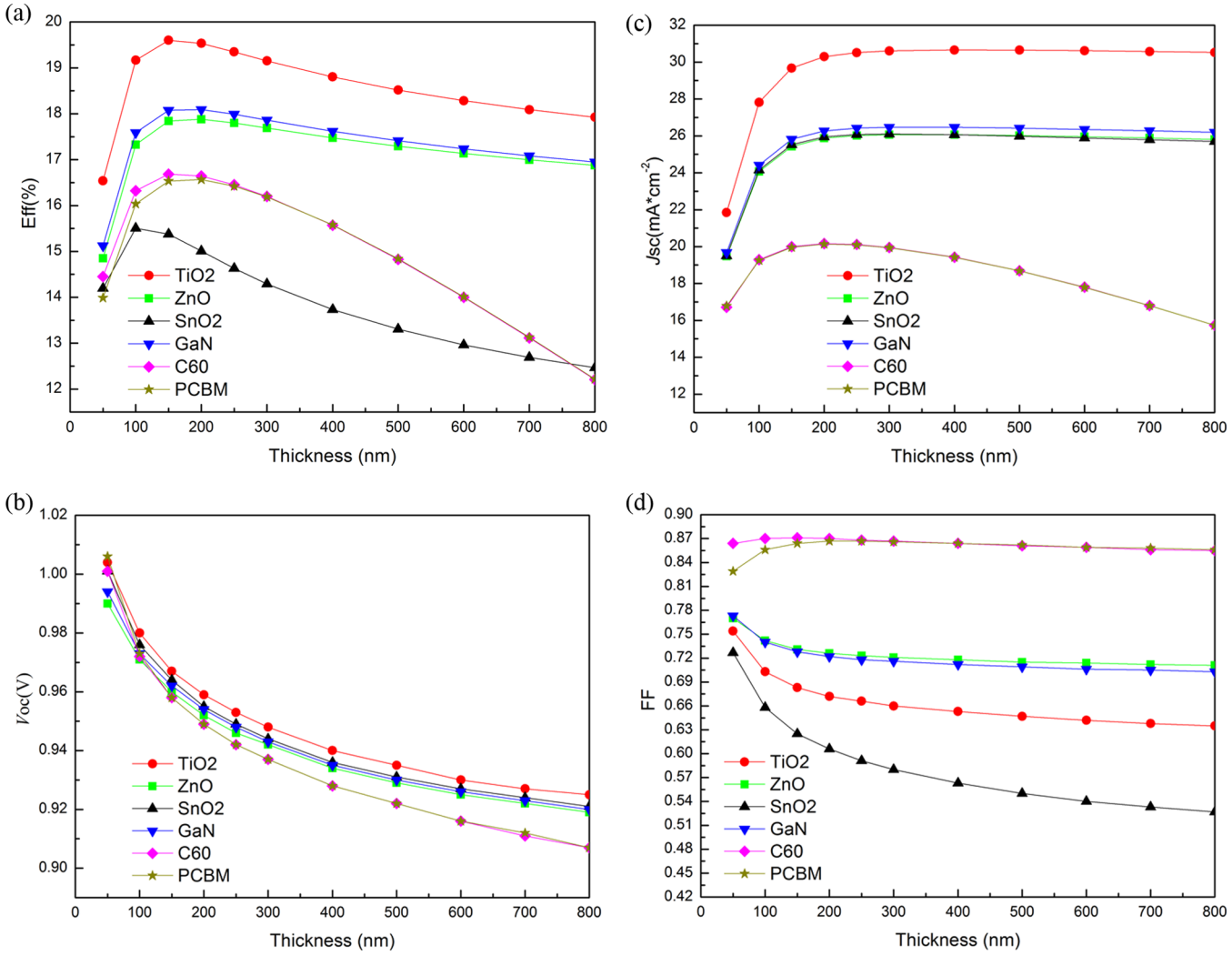

Figure 3. Photovoltaic performance of $CsSnI_3$ PSCs as functions of the thickness of $CsSnI_3$ absorbers eff (a), V_{oc} (b), J_{sc} (c), and FF (d).

3.2. Effect of the Thickness of Absorbers. Variation of PSC performance with the thickness of $CsSnI_3$ absorbers is shown in Figure 3. The shape of efficiency curves is similar for all of the ETLs (TiO_2, ZnO, SnO_2, GaN, C_{60}, and PCBM), and the same is true for open-circuit voltages (V_{oc}) curves and short-circuit current density (J_{sc}) curves. The efficiencies increase more or less steeply up to 100−200 nm and then decrease up to 800 nm (the efficiencies for SnO_2, C_{60}, and PCBM decrease sharply up to 800 nm). The PSCs with SnO_2 exhibit the lowest efficiencies in all of the simulated PSCs. It is attributed to their cliff-like band offsets at the $SnO_2/CsSnI_3$ interface (see Figure 2), which give rise to high interface-related recombination and low fill factor (FF).[23] When the thickness of absorbers ($CsSnI_3$) increases, recombination in the absorbers and reverse saturated current increases. Therefore, V_{oc} decreases with increasing $CsSnI_3$ thickness. The regular structures have larger J_{sc}. The J_{sc} increases more or less steeply up to 100−200 nm, which is attributed to the increased optical absorption and photogenerated carriers. When the thickness of absorbers increases further (>200 nm), J_{sc} tends to be saturated (for the regular structures) or decreases (for the inverted structures). It is because the recombination and series resistance increases when the thickness of absorbers increases. For the regular structures, FF decreases with the increasing thickness of absorbers, which is also due to the increased recombination and series resistance. The simulated results show that the inverted structures have larger FF than the regular structures. The optimal thickness of PSCs with TiO_2, ZnO, SnO_2, GaN, C_{60}, and PCBM is 150, 200, 100, 200, 150, and 200 nm, respectively. The optimal thickness of absorbers is in the range of 100−200 nm, which is consistent with some experimental reports.[6,24−26] In this work, the hole mobility of 400 $cm^2/V/s$[7] was used for $CsSnI_3$, which was obtained from transport property measurements. If the calculated hole mobility of 585 $cm^2/V/s$[7] is used, the optimal thickness of $CsSnI_3$ absorbers should be longer. In the following sections, the thickness of $CsSnI_3$ absorbers is set as the optimal thickness for all of the simulated PSCs.

3.3. Effect of the Thickness and Dopant Concentrations of ETLs. Figure 4 is the plot of the efficiency and J_{sc} versus the thickness of ETLs. The figure shows that the efficiency and J_{sc} are not very sensitive to the thickness of the ETLs. For example, the efficiency of PSCs with TiO_2 gradually decreases from 19.61 to 19.534% and J_{sc} gradually decreases from 29.689 to 29.532 mA/cm^2 due to the fractional absorption of incident light by the ETLs and increase in series resistance. V_{oc} and FF remain almost the same when the thickness of the ETLs increases. For simplicity, the thickness of the ETLs is set as 30 nm for all of the simulated PSCs.

https://doi.org/10.1021/acsomega.1c04096
ACS Omega 2021, 6, 26689−26698

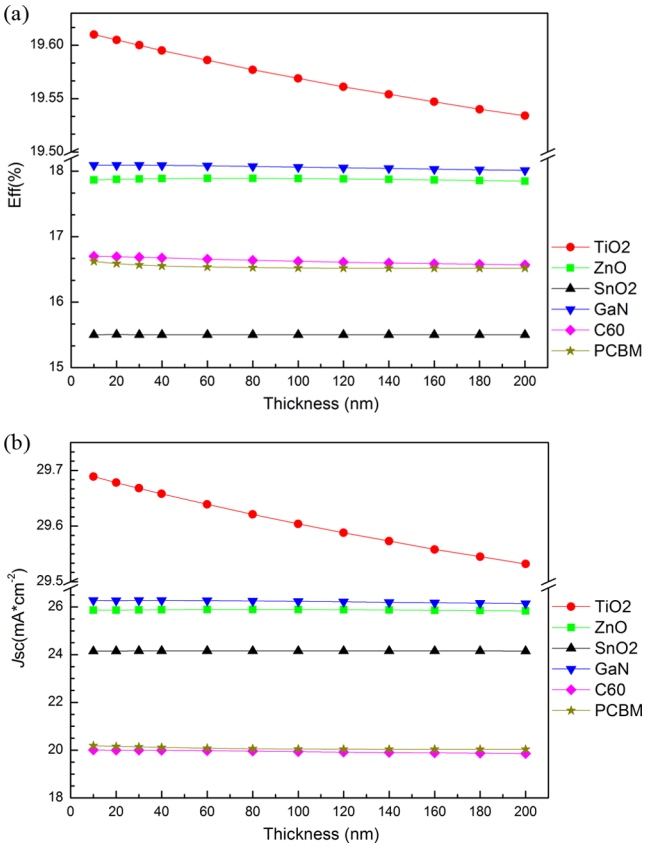

Figure 4. Efficiency (a) and J_{sc} (b) of $CsSnI_3$ PSCs as functions of the thickness of ETLs.

Figure 5 shows the PV cell parameters as functions of dopant concentrations (N_D). In the figure, N_D is set below the density of states in the conduction band of ETLs, and the barrier height of the ETL/electrode contact ($q\phi_m = E_c - E_f$) is set to make a flat band. For the regular structures, the PV parameters (efficiency, J_{sc}, and FF) are enhanced (slightly) with increasing dopant concentrations due to the increase in the conductivity of ETLs. For the inverted structures, the PV parameters (efficiency, V_{oc}, and FF) increase slightly first and then decrease. The decrease of PV parameters may be attributed to the change of band structures caused by the increased dopant concentrations and has been observed in the experiment for the inverted $MAPbI_3$ PSCs.[27] In the following sections, the dopant concentrations are set as the optimal concentrations (see Table S1) for all of the simulated PSCs. For the inverted $CsSnI_3$ PSCs, the optimal donor concentrations of ETLs are about 5×10^{18} cm^{-3}.

3.4. Comparison of Photovoltaic Performance for the Best Structures. The best photovoltaic performance and optimal device parameters of all of the simulated PSCs are shown in Figure 6 and Table 1, respectively. From the figure and table, the regular structures have higher J_{sc} than the inverted structures, but the inverted structures have a larger FF. All of the simulated optimal PSCs have similar V_{oc}. The optimal PSC with TiO_2 exhibits the highest efficiency of 20.131%, and the optimal PSC with SnO_2 exhibits the lowest efficiency of 15.504%. It could be concluded that there should not be spike-like or cliff-like band offsets in the conduction band at the ETL/$CsSnI_3$ interface to obtain high performance. The band gap and electron affinity of TiO_2, ZnO, and GaN are very close, but it is noted that TiO_2 has a large dielectric constant of 55,[28] which is much higher than that of ZnO (8.656[29]) and GaN (9.5[30]). Some groups[31−33] have investigated experimentally how ETLs with different dielectric constants affect the performance of organic−inorganic hybrid PSCs. They found that the dielectric constant of ETLs plays an important role in preventing electron−hole recombination in PSCs and the device performance could be improved with the increased dielectric constant of ETLs.[31−33] The photovoltaic performance of PSC with C_{60} is slightly better than that of PSC with PCBM. It is partly attributed to the fact that the carrier mobility of C_{60} (1.6 $cm^2/V/s$[34]) is higher than that of PCBM (0.01 $cm^2/V/s$[35]).

All of the simulated optimal PSCs with diverse electron-transporting materials (both regular and inverted planar structures) exhibit a similar V_{oc} of ∼0.96 V. However, in practice, low V_{oc} (<0.6 V) was reported in most of the experimental $CsSnI_3$ PSCs,[36−38] which is far behind the band gap (1.3 eV) of $CsSnI_3$ absorbers. For comparison, the V_{oc} exceeding 1.26 V could be achieved with its band gap of 1.55 eV for $MAPbI_3$ PSCs.[39] In the research field of $CsSnI_3$ PSCs, the most crucial goal is to develop efficient strategy to improve V_{oc} of the devices, and more fundamental studies are required to understand the origin of low V_{oc}.[38] It can be seen from Figure 9b that the interface trap at the ETLs/$CsSnI_3$ interface could cause a significant drop in V_{oc} when the interface trap density and capture cross section are large. From the simulation results and other experimental reports,[12,13,38] it could be concluded that the low crystal quality of $CsSnI_3$ thin films and the interface quality may mainly be responsible for the low V_{oc} in $CsSnI_3$ PSCs. Defects in the $CsSnI_3$ films and interface trap could increase recombination and reverse saturation current, and thus reduce V_{oc}. Li et al.[12] reported (January 2021) that an obvious V_{oc} enhancement from 0.47 to 0.63 V is achieved by reducing deep level trap-state density with the surface passivation of thiosemicarbazide. Ye et al.[13] (March 2021) found that the undesirable oxidation in $CsSnI_3$ is restricted by engineering the localized electron density with a phthalimide (PTM) additive and demonstrated that the lone electron pairs of NH and two CO functional groups in the PTM form coordination interactions with Sn^{2+} in the $CsSnI_3$ and protect it from oxidation to Sn^{4+}. Their $CsSnI_3$-PTM device exhibited an overall PCE of 10.1% with a V_{oc} of 0.64 V.

The quantum efficiencies (QEs) or spectral responses of all of the simulated PSCs are shown in Figure 7. In the near-infrared region, the quantum efficiencies of the PSCs decrease sharply at about 950 nm, which corresponds to the band gap of $CsSnI_3$ thin film. PSC with TiO_2 exhibits the highest quantum efficiency (∼0.88) in the visible region. The inverted structures with C_{60} and PCBM exhibit the lowest quantum efficiency (∼0.59) in the visible region and thus the lowest J_{sc}.

Figure 8 shows the quantum efficiencies of TiO_2/$CsSnI_3$/Spiro-OMeTAD PSCs versus the thickness of $CsSnI_3$ absorbers. The quantum efficiencies increase steeply when the thickness of the absorber increases from 50 to 100 nm due to the increased optical absorption and photogenerated carriers. It tends to be saturated when the thickness of the absorber increases above 200 nm, which is because the recombination increases (so the collection efficiency decreases) and series resistance increases. When the thickness of $CsSnI_3$ is 150 nm, the optimal TiO_2/$CsSnI_3$/Spiro-OMeTAD PSC exhibits the highest efficiency of 20.131% (J_{sc} = 29.673 mA/cm^2).

3.5. Effect of the Interface Trap Density of States. The nanoscale interface states play an important role in the device performance.[40] In the device simulation, the effects of the interface trap density of states are also studied by introducing a 5

https://doi.org/10.1021/acsomega.1c04096
ACS Omega 2021, 6, 26689−26698

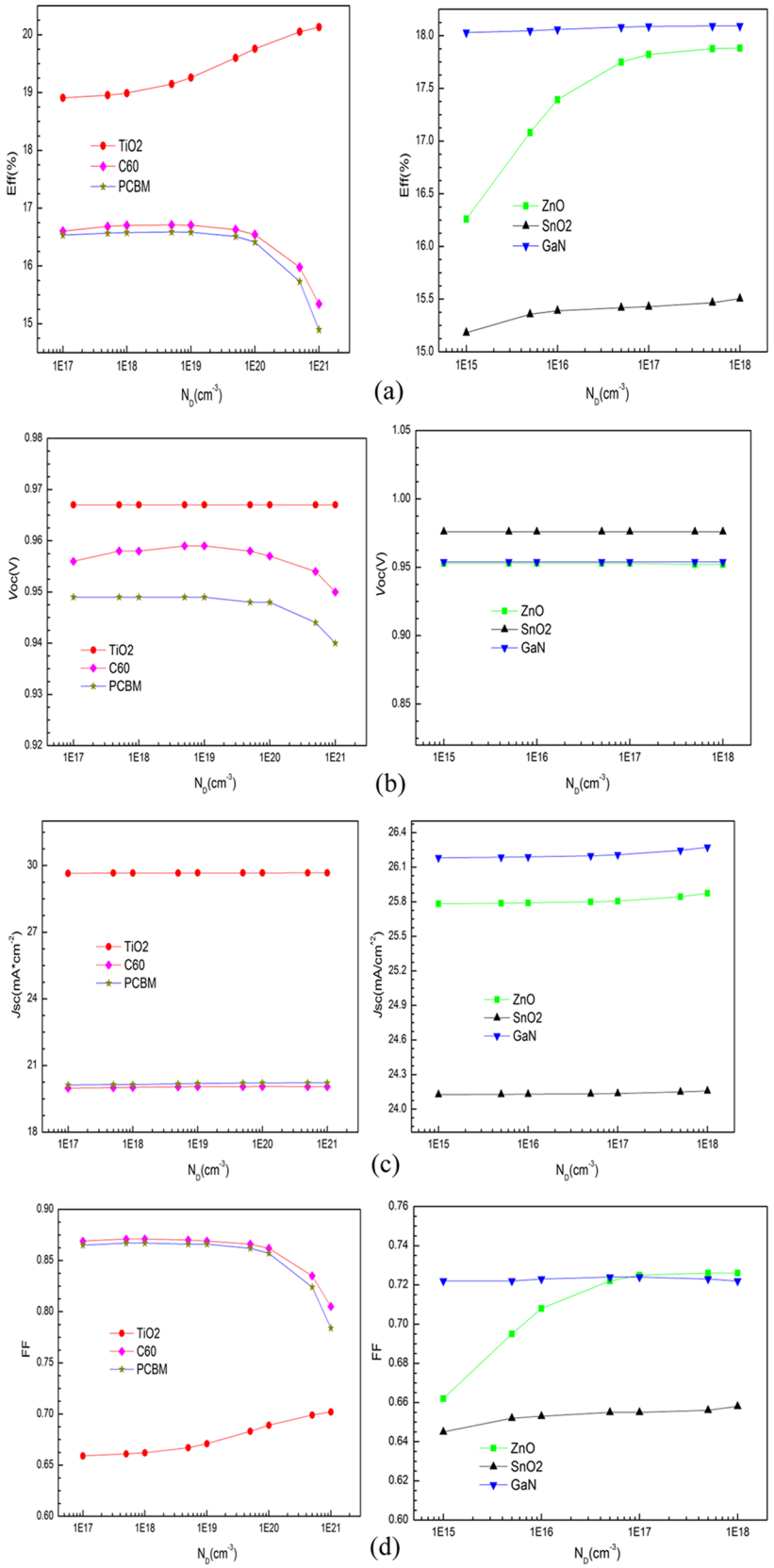

Figure 5. Photovoltaic performance of $CsSnI_3$ PSCs as functions of dopant concentrations (N_D) eff (a), V_{oc} (b), J_{sc} (c), and FF (d).

nm interface defect layer (IDL) at the $TiO_2/CsSnI_3$ interface for $TiO_2/CsSnI_3$/Spiro-OMeTAD PSCs. Figure 9 shows the plot of PV cell parameters as functions of the interface trap density and capture cross section. From the figure, the interface trap has an important influence on efficiency, V_{oc}, J_{sc}, and FF. It is clear that efficiency, V_{oc}, J_{sc}, and FF decrease with increasing interface trap density and capture cross section. When the capture cross sections are 10^{-18} and 10^{-17} cm^2, the efficiencies decrease slowly

https://doi.org/10.1021/acsomega.1c04096
ACS Omega 2021, 6, 26689−26698

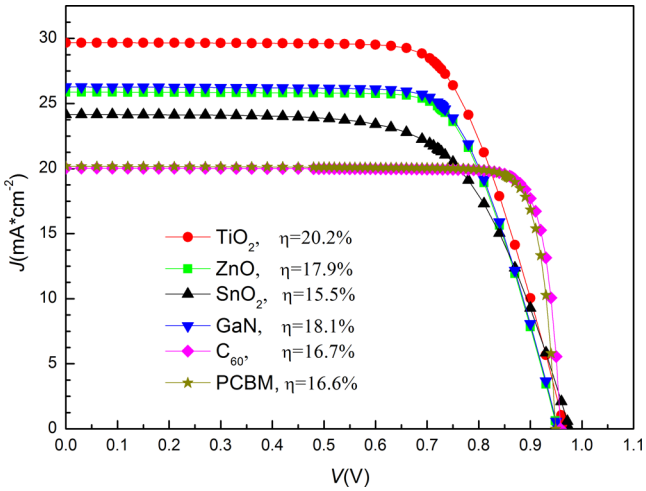

Figure 6. Photovoltaic performance of optimal $CsSnI_3$ PSCs.

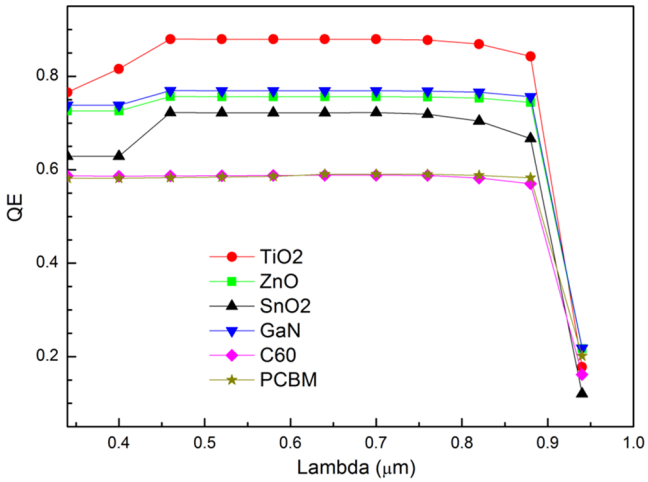

Figure 7. Quantum efficiencies of optimal $CsSnI_3$ PSCs.

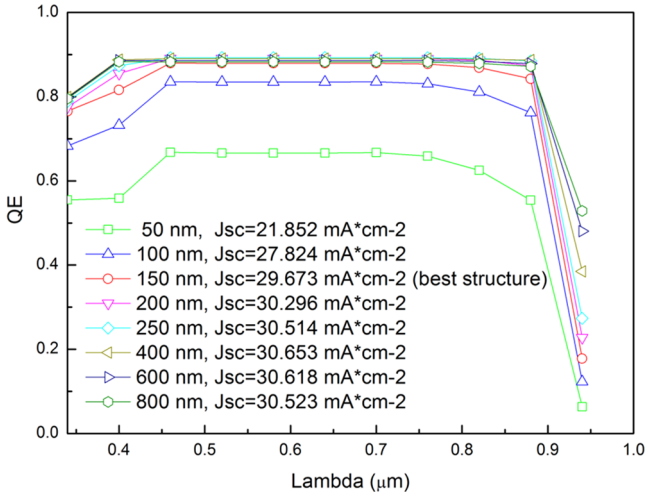

Figure 8. Quantum efficiencies of $TiO_2/CsSnI_3$/Spiro-OMeTAD PSCs versus the thickness of $CsSnI_3$ absorbers.

from 19.825 to 19.424% and 16.798%, respectively. However, when the capture cross section increases to 10^{-15} and 10^{-14} cm^2, the efficiency decreases sharply to 3.232 and 0.154%, respectively. Interface trap and large capture cross section increase the recombination centers and hence change in shunt resistance. Optimizing the doping of the ETL and formation of a flat, smooth, and homogeneous surface will significantly reduce the interface trap density and hence enhance the performance. The recombination mechanisms of photocarriers at the ETL/perovskite interfaces could be found in the literature, such as refs41, 42.

4. CONCLUSIONS

B-γ-$CsSnI_3$ has attracted considerable attention as a promising inorganic, lead-free, thermally stable perovskite for next-generation PSCs due to its favorable photoelectric properties. In this work, $CsSnI_3$ PSCs with diverse ETLs (TiO_2, ZnO, SnO_2, GaN, C_{60}, and PCBM) were simulated. Effects of the thickness of $CsSnI_3$ absorbers and ETLs, dopant concentration of ETLs, and interface trap density of states on the photovoltaic performance of PSCs were investigated to find the optimal device structures. The optimal thickness of $CsSnI_3$ absorbers is in the range of 100−200 nm (the hole mobility of 400 $cm^2/V/s$[7] was used for $CsSnI_3$, which was obtained from transport property measurements). The regular structures have larger J_{sc} than the inverted structures, but the inverted structures have larger FF. All of the simulated optimal PSCs exhibit a similar V_{oc} of ∼0.96 V.

It was found that the photovoltaic performance of $CsSnI_3$ PSCs is not very sensitive to the thickness of the ETLs. The optimal thickness of ETLs is about 20−30 nm. For the regular structures, the PV parameters (efficiency, J_{sc}, and FF) are enhanced (slightly) with increasing dopant concentrations of ETLs due to the increase in the conductivity of ETLs. For the inverted structures, the PV parameters (efficiency, V_{oc}, and FF) increase slightly first and then decrease with increasing dopant concentrations of ETLs. The optimal donor concentrations of ETLs are about 5×10^{18} cm^{-3} for the inverted structures. It was found that TiO_2 is the best electron-transporting material in all of the simulated ETLs. When the thickness of $CsSnI_3$ is 150 nm, the optimal $TiO_2/CsSnI_3$/Spiro-OMeTAD PSC exhibits the highest efficiency of 20.2% with a V_{oc} of 0.97 V, J_{sc} of 29.67 mA/cm^2, and FF of 0.70. The optimal PSCs with ZnO, GaN, C_{60}, and PCBM ETLs exhibit efficiencies of 17.88, 18.09, 16.71, and

Table 1. Best Photovoltaic Performance and Optimal Device Parameters of $CsSnI_3$ PSCs

PSC with ETL	TiO_2	ZnO	SnO_2	GaN	C_{60}	PCBM
thickness of $CsSnI_3$ absorber (nm)	150	200	100	200	150	200
thickness of ETL (nm)	30	30	30	30	30	30
donor concentration N_D (cm^{-3})	1.00×10^{21}	1.00×10^{18}	1.00×10^{18}	1.00×10^{18}	5.00×10^{18}	5.00×10^{18}
eff (%)	20.131	17.882	15.504	18.091	16.711	16.589
V_{oc} (V)	0.967	0.952	0.976	0.954	0.959	0.949
J_{sc} (mA/cm^2)	29.673	25.874	24.158	26.273	20.037	20.177
FF	0.702	0.726	0.658	0.722	0.87	0.866

https://doi.org/10.1021/acsomega.1c04096
ACS Omega 2021, 6, 26689−26698

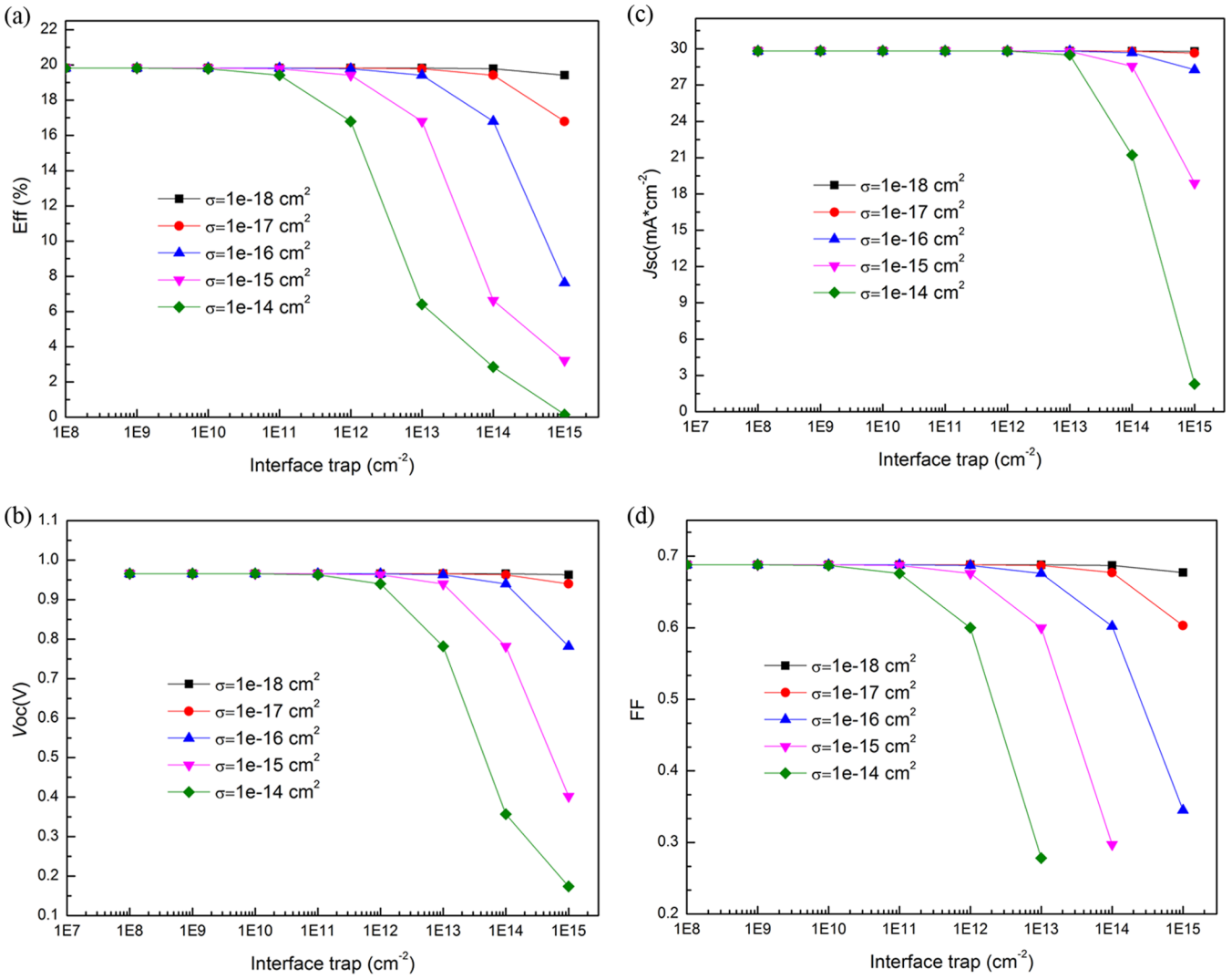

Figure 9. Photovoltaic performance of TiO_2/$CsSnI_3$/Spiro-OMeTAD PSCs as functions of the interface trap density and capture cross section eff (a), V_{oc} (b), J_{sc} (c), and FF (d).

16.59%, respectively. The optimal PSC with SnO_2 ETL exhibits the lowest efficiency of 15.5% in all of the simulated PSCs due to its cliff-like band offset at the SnO_2/$CsSnI_3$ interface. It could be concluded that there should not be spike-like or cliff-like band offsets in the conduction band at the ETL/$CsSnI_3$ interface to obtain high performance. Furthermore, the photovoltaic performance of PSCs was found to degrade with increasing interface trap density and capture cross section.

■ ASSOCIATED CONTENT

Supporting Information

The Supporting Information is available free of charge at https://pubs.acs.org/doi/10.1021/acsomega.1c04096.

Material parameters of $CsSnI_3$, ETLs, and HTLs used in the simulations (Table S1) and band alignment of all contact materials and $CsSnI_3$ adopted in this study (Figure S1) (PDF)

■ AUTHOR INFORMATION

Corresponding Author

Jin-Cheng Zheng − *Collaborative Innovation Center for Optoelectronic Semiconductors and Efficient Devices, Department of Physics, Xiamen University, Xiamen 361005, People's Republic of China; Department of Physics, Xiamen University Malaysia, Sepang 43900 Selangor, Malaysia*; Email: jczheng@xmu.edu.cn

Authors

Shuo Lin − *College of Physics and Information Engineering, Minnan Normal University, Zhangzhou 363000 Fujian, People's Republic of China*; orcid.org/0000-0003-0359-6439

Baoping Zhang − *Department of Electronic Engineering, Optoelectronics Engineering Research Center, College of Electronic Science and Technology (National Model Microelectronics College), Xiamen University, Xiamen 361005, People's Republic of China*

Tie-Yu Lü − *Collaborative Innovation Center for Optoelectronic Semiconductors and Efficient Devices, Department of Physics, Xiamen University, Xiamen 361005, People's Republic of China*

Huaqing Pan − *Department of Mechanical Engineering, Shangrao Vocational and Technical College, Shangrao 334109 Jiangxi, People's Republic of China*

https://doi.org/10.1021/acsomega.1c04096
ACS Omega 2021, 6, 26689−26698

Huanting Chen − *College of Physics and Information Engineering, Minnan Normal University, Zhangzhou 363000 Fujian, People's Republic of China*
Chuanjin Lin − *College of Physics and Information Engineering, Minnan Normal University, Zhangzhou 363000 Fujian, People's Republic of China*
Xirong Li − *College of Physics and Information Engineering, Minnan Normal University, Zhangzhou 363000 Fujian, People's Republic of China*
Jinrong Zhou − *College of Physics and Information Engineering, Minnan Normal University, Zhangzhou 363000 Fujian, People's Republic of China*

Complete contact information is available at: https://pubs.acs.org/10.1021/acsomega.1c04096

Author Contributions

The manuscript was written through the contributions of all authors. All authors have given approval to the final version of the manuscript.

Notes

The authors declare no competing financial interest.

■ ACKNOWLEDGMENTS

This work is supported by the Xiamen University Malaysia Research Fund (No. XMUMRF/2019-C3/IORI/0001), the Education Department of Fujian Province JK Project (No. JK2017033), Minnan Normal University Project (Nos. HX2019077 and XJZ18046), National Natural Science Foundation of China (No. 61975072), Industry-University-Research Collaboration Foundation of the Fujian Province (No. 2020H6017), and Program for Innovative Research Team in Science and Technology in Fujian Province University (Optoelectronic Materials and Device Application). The authors would like to thank the Fonash Research Group in the Pennsylvania State University for providing the AMPS-1D simulation package.

■ REFERENCES

(1) Lee, M. M.; Teuscher, J.; Miyasaka, T.; Murakami, T. N.; Snaith, H. J. Efficient hybrid solar cells based on meso-superstructured organometal halide perovskites. *Science* **2012**, *338*, 643−647.
(2) Jeong, J.; Kim, M.; Seo, J.; Lu, H.; Ahlawat, P.; Mishra, A.; Yang, Y.; Hope, M. A.; Eickemeyer, F. T.; Kim, M.; Yoon, Y. J.; Choi, I. W.; Darwich, B. P.; Choi, S. J.; Jo, Y.; Lee, J. H.; Walker, B.; Zakeeruddin, S. M.; Emsley, L.; Rothlisberger, U.; Hagfeldt, A.; Kim, D. S.; Grätzel, M.; Kim, J. Y. Pseudo-halide anion engineering for α-FAPbI3 perovskite solar cells. *Nature* **2021**, *592*, 381−385.
(3) Ishikawa, R.; Watanabe, S.; Yamazaki, S.; Oya, T.; Tsuboi, N. Perovskite/graphene solar cells without a hole-transport layer. *ACS Appl. Energy Mater.* **2019**, *2*, 171−175.
(4) Tessler, N.; Vaynzof, Y. Preventing hysteresis in perovskite solar cells by undoped charge blocking layers. *ACS Appl. Energy Mater.* **2018**, *1*, 676−683.
(5) Shalenov, E. O.; Dzhumagulova, K. N.; Seitkozhanov, Y. S.; Ng, A.; Valagiannopoulos, C.; Jumabekov, A. N. Insights on desired fabrication factors from modeling sandwich and quasi-interdigitated back-contact perovskite solar cells. *ACS Appl. Energy Mater.* **2021**, *4*, 1093−1107.
(6) Wang, N.; Zhou, Y.; Ju, M.; Garces, H. F.; Ding, T.; Pang, S.; Zeng, X. C.; Padture, N. P.; Sun, X. W. Heterojunction-depleted lead-free perovskite solar cells with coarse-grained B-γ-CsSnI3 thin films. *Adv. Energy Mater.* **2016**, *6*, No. 1670137.
(7) Chung, I.; Song, J. H.; Im, J.; Androulakis, J.; Malliakas, C. D.; Li, H.; Freeman, A. J.; Kenney, J. T.; Kanatzidis, M. G. CsSnI3: semiconductor or metal? High electrical conductivity and strong near-infrared photoluminescence from a single material. High hole mobility and phase-transitions. *J. Am. Chem. Soc.* **2012**, *134*, 8579−8587.
(8) Minemoto, T.; Murata, M. Device modeling of perovskite solar cells based on structural similarity with thin film inorganic semiconductor solar cells. *J. Appl. Phys.* **2014**, *116*, No. 054505.
(9) Chung, I.; Lee, B.; He, J.; Chang, R. P. H.; Kanatzidis, M. G. All-solid-state dye-sensitized solar cells with high efficiency. *Nature* **2012**, *485*, 486−489.
(10) Ma, S.; Gu, X.; Kyaw, A. K.; Wang, D. H.; Priya, S.; Ye, T. Fully Inorganic CsSnI3-based solar cells with>6% efficiency and enhanced stability enabled by mixed electron transport layer. *ACS Appl. Mater. Interfaces* **2021**, *13*, 1345−1352.
(11) Wang, Y.; Tu, J.; Li, T.; Tao, C.; Deng, X.; Li, Z. Convenient preparation of CsSnI3 quantum dots, excellent stability, and the highest performance of lead-free inorganic perovskite solar cells so far. *J. Mater. Chem. A* **2019**, *7*, 7683−7690.
(12) Li, B.; Di, H.; Chang, B.; Yin, R.; Fu, L.; Zhang, Y.; Yin, L. Efficient passivation strategy on Sn related defects for high performance all-inorganic CsSnI3 perovskite solar cells. *Adv. Funct. Mater.* **2021**, *31*, No. 2007447.
(13) Ye, T.; Wang, X.; Wang, K.; Ma, S.; Yang, D.; Hou, Y.; Yoon, J.; Wang, K.; Priya, S. Localized electron density engineering for stabilized B-γ CsSnI3-based perovskite solar cells with efficiencies >10%. *ACS Energy Lett.* **2021**, *6*, 1480−1489.
(14) Adhikari, K. R.; Gurung, S.; Bhattarai, B. K.; Soucase, B. M. Comparative study on MAPbI3 based solar cells using different electron transporting materials. *Phys. Status Solidi C* **2016**, *13*, 13−17.
(15) Etgar, L.; Gao, P.; Xue, Z. S.; Peng, Q.; Chandiran, A. K.; Liu, B.; Nazeeruddin, M. K.; Grätzel, M. Mesoscopic CH3NH3PbI3/TiO2 heterojunction solar cells. *J. Am. Chem. Soc.* **2012**, *134*, 17396−17399.
(16) Laban, W. A.; Etgar, L. Depleted hole conductor-free lead halide iodide heterojunction solar cells. *Energy Environ. Sci.* **2013**, *6*, 3249−3253.
(17) Aharon, S.; Gamliel, S.; El Cohen, B.; Etgar, L. Depletion region effect of highly efficient hole conductor free CH3NH3PbI3 perovskite solar cells. *Phys. Chem. Chem. Phys.* **2014**, *16*, 10512−10518.
(18) Aharon, S.; El Cohen, B.; Etgar, L. Hybrid lead halide iodide and lead halide bromide in efficient hole conductor free perovskite solar cell. *J. Phys. Chem. C* **2014**, *118*, 17160−17165.
(19) Xiao, L. X.; Zou, D. C. *Perovskite Solar Cells*, 2nd ed.; Peking University Press, 2020.
(20) Chen, J. Y.; Chen, F. X.; Xu, W. K.; Cao, G. H.; Wang, L. S. Simulation optimization of planar heterojunction perovskite solar cells with B-γ-CsSnI3 as optical absorption layer. *J. Synth. Cryst.* **2018**, *47*, 31−36.
(21) Fonash, S. J. et al. AMPS Manual, 2010. http://www.ampsmodeling.org/pdfs/AMPS-1D%20Manual.pdf.
(22) Lin, S.; Li, X. R.; Pan, H. Q.; Chen, H. T.; Li, X. Y.; Li, Y.; Zhou, J. R. Numerical analysis of InxGa1-xN/SnS and AlxGa1-xN/SnS heterojunction solar cells. *Energy Convers. Manage.* **2016**, *119*, 361−367.
(23) Ghorbani, E. On efficiency of earth-abundant chalcogenide photovoltaic materials buffered with CdS: the limiting effect of band alignment. *J. Phys.: Energy* **2020**, *2*, No. 025002.
(24) Marshall, K. P.; Walton, R. I.; Hatton, R. A. Tin perovskite/fullerene planar layer photovoltaics: improving the efficiency and stability of lead-free devices. *J. Mater. Chem. A* **2015**, *3*, 11631−11640.
(25) Marshall, K. P.; Walker, M.; Walton, R. I.; Hatton, R. A. Enhanced stability and efficiency in hole-transport-layer-free CsSnI3 perovskite photovoltaics. *Nat. Energy* **2016**, *1*, No. 16178.
(26) Wu, B.; Zhou, Y.; Xing, G.; Xu, Q.; Garces, H. F.; Solanki, A.; Goh, T. W.; Padture, N. P.; Sum, T. C. Long minority-carrier diffusion length and low surface-recombination velocity in inorganic lead-free CsSnI3 perovskite crystal for solar cells. *Adv. Funct. Mater.* **2017**, *27*, No. 1604818.
(27) Bin, Z.; Li, J.; Wang, L.; Duan, L. Efficient n-type dopants with extremely low doping ratios for high performance inverted perovskite solar cells. *Energy Environ. Sci.* **2016**, *9*, 3424−3428.

(28) vande Krol, R.; Goossens, A.; Schoonman, J. Mott-Schottky analysis of nanometer-scale thin-film anatase TiO2. *J. Electrochem. Soc.* **1997**, *144*, 1723−1727.
(29) Pearton, S. J.; Norton, D. P.; Ip, K.; Heo, Y. W.; Steiner, T. Recent progress in processing and properties of ZnO. *Superlattices Microstruct.* **2003**, *34*, 3−32.
(30) Lin, S.; Zeng, S. W.; Cai, X. M.; Zhang, J. Y.; Wu, S. X.; Sun, L.; Zhang, B. P. Simulation of doping levels and deep levels in InGaN-based single-junction solar cell. *J. Mater. Sci.* **2012**, *47*, 4595−4603.
(31) Shao, S.; Abdu-Aguye, M.; Qiu, L.; Lai, L. H.; Liu, J.; Adjokatse, S.; Jahani, F.; Kamminga, M. E.; ten Brink, G. H.; Palstra, T. T. M.; Kooi, B. J.; Hummelenab, J. C.; Loi, M. A. Elimination of the light soaking effect and performance enhancement in perovskite solar cells using a fullerene derivative. *Energy Environ. Sci.* **2016**, *9*, 2444−2452.
(32) Castro, E.; Fernandez-Delgado, O.; Arslan, F.; Zavala, G.; Yang, T.; Seetharaman, S.; D'Souza, F.; Echegoyen, L. New thiophene-based C60 fullerene derivatives as efficient electron transporting materials for perovskite solar cells. *New J. Chem.* **2018**, *42*, 14551−14558.
(33) Shao, S.; Liu, J.; Fang, H. H.; Qiu, L.; ten Brink, G. H.; Hummelen, J. C.; Koster, L. J. A.; Loi, M. A. Efficient perovskite solar cells over a broad temperature window: the role of the charge carrier extraction. *Adv. Energy Mater.* **2017**, *7*, No. 1701305.
(34) Golubev, T.; Liu, D.; Lunt, R.; Duxbury, P. Understanding the impact of C60 at the interface of perovskite solar cells via drift-diffusion modeling. *AIP Adv.* **2019**, *9*, No. 035026.
(35) Zhao, P.; Liu, Z.; Lin, Z.; Chen, D.; Su, J.; Zhang, C.; Zhang, J.; Chang, J.; Hao, Y. Device simulation of inverted CH3NH3PbI3−xClx perovskite solar cells based on PCBM electron transport layer and NiO hole transport layer. *Sol. Energy* **2018**, *169*, 11−18.
(36) Tai, Q.; Tang, K.-C.; Yan, F. Recent progress of inorganic perovskite solar cells. *Energy Environ. Sci.* **2019**, *12*, 2375−2405.
(37) Konstantakou, M.; Stergiopoulos, T. A critical review on tin halide perovskite solar cells. *J. Mater. Chem. A* **2017**, *5*, 11518−11549.
(38) Gao, W.; Li, P.; Chen, J.; Ran, C.; Wu, Z. Interface engineering in tin perovskite solar cells. *Adv. Mater. Interfaces* **2019**, *6*, No. 1901322.
(39) Liu, Z.; Krückemeier, L.; Krogmeier, B.; Klingebiel, B.; Márquez, J. A.; Levcenko, S.; Öz, S.; Mathur, S.; Rau, U.; Unold, T.; Kirchartz, T. Open-circuit voltages exceeding 1.26 V in planar methylammonium lead iodide perovskite solar cells. *ACS Energy Lett.* **2019**, *4*, 110−117.
(40) Wang, H.-Q.; Xu, J.; Lin, X.; Li, Y.; Kang, J.; Zheng, J.-C. Determination of the embedded electronic states at nanoscale interface via surface-sensitive photoemission spectroscopy. *Light: Sci. Appl.* **2021**, *10*, No. 153.
(41) Le Corre, V. M.; Stolterfoht, M.; Toro, L. P.; Feuerstein, M.; Wolff, C.; Gil-Escrig, L.; Bolink, H. J.; Neher, D.; Koster, L. J. A. Charge transport layers limiting the efficiency of perovskite solar cells: how to optimize conductivity, doping, and thickness. *ACS Appl. Energy Mater.* **2019**, *2*, 6280−6287.
(42) Hu, J.; Gouda, L.; Kama, A.; Tirosh, S.; Gottesman, R. Radiative recombination changes under light-soaking in CsPbBr3 films on TiO2 and insulating glass contacts: interface versus bulk effects. *ACS Appl. Energy Mater.* **2019**, *2*, 3013−3016.

https://doi.org/10.1021/acsomega.1c04096
ACS Omega 2021, 6, 26689−26698